Different methods of measuring synergy between cavitation erosion and corrosion for nickel aluminium bronze in 3.5% NaCl solution

J. Basumatary[1], R. J. K. Wood[1]
[1]University of Southampton, SO17 1BJ, United Kingdom

Abstract

In order to understand the combined detrimental effects of cavitation erosion and corrosion in seawater on a conventional marine alloy, nickel aluminium bronze, five different methods were employed to obtain synergism. The experiments were conducted using an ultrasonic vibratory horn functioning at 19.5 kHz frequency and 80 μm ± 0.2 μm peak-to-peak amplitude. The test methods used to obtain the synergy included gravimetric mass loss technique, volumetric mass loss and mean depth of penetration rate methods, and polarization technique. The cavitated surfaces were microstructurally characterized via scanning electron microscopy. Synergism was found to have measurable impact on the cavitation erosion-corrosion of NAB, with its microstructure undergoing selective phase attack, resulting in increased material removal especially in the presence of corrosive environment.

Keywords: cavitation; erosion; tribo-corrosion; synergism;

1. Introduction

Cavitation occurs when a liquid reaches its boiling point, even at ambient temperatures, when its absolute pressure drops below its vapour pressure, causing the liquid to vaporize and produce cavities. These cavities grow rapidly and collapse asymmetrically, forming small diameter (~10 μm) microjets impinging at a speed up to 200 m s^{-1} [1]. This in turn creates spots of very high water hammer and stagnation pressure. Bubble collapse can create instantaneous temperature at the bubble centre reaching as high as 8500 °C [2], emitting destructive shock waves [3], [4]. It has various detrimental consequences such as pitting, surface wear, micro-cracking, noise, sonoluminescence, and corrosion if at a close vicinity to a solid surface [5], [6].

Cavitation erosion is a fluid-to-surface type of erosion that occurs when a portion of the fluid is first exposed to tensile stresses that cause the fluid to boil, then exposed to compressive stresses that cause the vapour bubbles to implode. It requires a high relative motion between the surface and the fluid. The implosion

produces shock waves and causes microjets to impinge against the surfaces. It is a tribo-corrosion phenomenon, which is a result of the combination of mechanical as well as electrochemical actions. Its complexity depends on the type and unsteadiness of cavitation, the response of the material to the cavitation energy imparted, and the surrounding corrosive environment [7], [8].

Bubble collapse causes surface/sub surface stresses. These stresses are generally enhanced at stress risers (notches, tears, welding defects, etc.) or at heterogeneous areas of the material such as at the directionality of metal flow, and can generate microcracks. These micro-cracks propagate to the point where the material can no longer withstand the impulse load that the imploding bubbles foist. Therefore, a rough surface is prone to cavitation erosion. And since pits and a rough profile characterize the cavitation damage, the damage increases as the surface becomes rougher [4].

Cavitation wear is mechanical in nature and cannot occur without the application of the tensile and compressive stresses. Cavitation wear damage undergoes several periods of activity. Depending on the surface structure, the material surface is deformed, loosened and eventually eroded in various ways due to the frequent strain from the shock waves. The rate of erosion is a function of the exposure period and it increases from negligible values, reaching a maximum before decreasing again and finally levelling off to a steady value[4], [9]–[11].

Marine propulsion systems are at an optimum risk of exposure to cavitation that essentially results in very expensive dry-docking, maintenance, repair, etc. Currently, nickel aluminium bronze (NAB), UNS C98500, is a conventional marine alloy used for the fabrication of marine propellers, due to its mechanical properties, and resistance towards corrosion in seawater [12], [13]. NAB gets its corrosion properties from a thick layer of protective oxide film predominantly composed of aluminium oxide (Al_2O_3) near the substrate with copper oxide (Cu_2O) formed mostly on the outer layer [52]. These films generally take several weeks immersed in seawater, depending on the environmental conditions, to reach a substantial thickness of up to 1 μm that will have a visible black/brown colouration over the alloy surface. They provide sufficient corrosion resistance, but may exhibit different corrosion behaviour for the NAB substrate when disrupted. However, the protective layer is not susceptible to localised breakdown and consequent pitting in the presence of chlorides, which makes NAB very resistant to corrosion by seawater [13], [53].

To understand the behaviour of NAB in different cavitation erosion and corrosion conditions, substantial studies have been done to understand its microstructural characteristics, and the relationship between cavitation erosion

and corrosion occurring in NAB [14]–[17]. This combined interaction between erosional aspects of cavitation and corrosion is termed as synergy. Several studies have been conducted and proven the existence of synergy between cavitation erosion and corrosion on marine materials such as stainless steel (SS), copper alloys, manganese bronze, and NAB among others [7], [18]–[30].

Synergy can be measured in terms of two common measurements, mass loss incurred by combined contribution of erosion and corrosion or the mean depth of penetration rate (MDPR). According to the ASTM G119 [31] guidelines for determining synergy during erosion–corrosion test, the equation for synergy is commonly written as Equation (1):

$$T = S + E + C \quad \ldots(1)$$

Where, T is the overall cavitation erosion-corrosion rate, C is pure corrosion contribution; E is the pure erosion contribution, and S the combined contribution due to synergistic effect. From Equation (1), S can be also represented as in Equation (2):

$$S = T - (E+C) = \Delta E + \Delta C \quad \ldots(2)$$

Where, ΔE = corrosion enhanced erosion, and ΔC = erosion enhanced corrosion.

It has raised curiosity in the recent years for its ability to correlate erosion and corrosion. At the same time it has also become a subject of debate whether the technique is suitable, as well as reproducible. Some authors have suggested that corrosion leads to increased abrasion resistance in some materials [32]–[35]. While, several authors mentioned the effect of corrosion on the rate of abrasion, generally leading to an increased weight loss [33], [36]–[38]. Most authors reported that abrasion increased the kinetics of corrosion [37]–[39]. Reports have also been made where the synergy results seemed to be dependent more on techniques and test conditions adopted during the tests as well as the impact of corrosive solution, the material property, and also the type of materials itself. For most alloys and metal samples the most significant impact was found at a mild corrosive environment [25], [26], [34], [40]–[44].

Tomlinson and Talks [35] studied the cavitation erosion–corrosion of various types of cast iron in 3% sodium chloride solution. The samples were eroded using a 20 kHz ultrasonic cavitation device at peak-to-peak amplitude of 15 μm in distilled water, increasing the salinity by 0.02% and 3%, at 50 °C. The standoff distance was kept constant at 1 mm. They found that the fractional weight loss due to pure corrosion ranged from 1% to 10% while that due to corrosion-induced erosion ranged from 16% to 90%.

Neville, Hodgkiess, et. al. [43], conducted an experiment on the synergy between the solid particle erosion-corrosion behaviour of engineering steels for marine pumping applications. They conducted a series of electromechanically based erosion tests under high-velocity (100 m s^{-l}) liquid impingement of 3.5% NaCl solution, and liquid-solid slurry impingement comprising of 3.5% NaCl and 1000 ppm cast silica sand flowing at 25 m s^{-1}. The materials used were C-Mn steel, UNS S31603 stainless steel and 2205 duplex stainless steel. The angle of impingement was 90°, whereas the temperature was kept constant at 50 °C in both cases. They concluded that corrosion had a significant effect on the material under the combined synergistic erosion-corrosion process. It was also found that increasing hardness yielded a lower total mass loss. However, these hardness correlations were not apparent when corrosion was under consideration.

In a study conducted by Bello, Wood and Wharton [34] on UNS S30403, S31603 and S32760 stainless steel, they attempted to evaluate the synergistic effects of micro-abrasion-corrosion using three approaches. They used two-body, mixed and three-body abrasion methods. They used SiC abrasives (with a mean particle size of 4.5 μm) in slurry. The slurries used were distilled water based for pure abrasion, and 3.5% NaCl solution based for abrasion-corrosion tests. The erosion test was conducted with a 22 mm diameter alumina ball in the micro-abrasion apparatus. The synergy resulting from a two-body wear mode was highly variable with a large degree of scatter. UNS S31603 and S32760 stainless steel gave negative synergy for two-body abrasion, while a positive synergy was seen for mixed and three-body abrasion. For S32760 stainless steel this result was attributed to its repassivation kinetics and/or the presence of a passive film. However, when the higher wear rate were reached, the film was ruptured or removed, leading to increase in the synergy. For S30403, only positive synergies were reported, attributing it to weak repassivation/passive oxide film structure.

The initial aim mainly was to study the quantification and sensitivity of synergism and antagonism between mechanical and electrochemical processes for air-filmed as-cast NAB.

Several variables and factors rendered accurate quantification of T, E and C difficult. And hence, the aim of the study was to perform different test methods in order to find the most reliable combination to obtain synergism found between erosion and corrosion for the test material. Furthermore, synergy is also highly dependent on the microstructure of the material, the environment, and the duration exposure, hence spatial and temporal aspects of Tribocorrosion testing must be considered. The cavitation experiments were conducted by means of an indirect ultrasonic vibratory system as presented in Ref [44] at room temperature.

2. Material and methodology

2.1 Test material

The test material used for the research was cast NAB C95800 (without heat treatment). The empirical composition of the cast NAB used is Cu-Al-Fe-Ni, with a nominal composition of 10% aluminium, 5% nickel and 5% iron. The alloy's property comes from a very complex network of microstructures. It generally consists of columnar grains of face centred cubic (FCC) copper-rich solid solution known as α-phase and a small volume fraction of β-phase or retained martensitic β'-phase, surrounded by a series of intermetallic Fe-rich kappa phases [14], [16], [44]–[46].

Among the intermetallic compounds, κ_I phase is rosette shaped precipitate formed at high temperatures in high Fe-content alloys and hence, is the coarsest among them ranging from 5 µm – 10 µm in diameter, κ_{II} phase is smaller than κ_I phase and form a dendritic rosette shape which is distributed mostly at the α/β boundaries, ranging from 1 µm – 2 µm in diameter, and κ_{IV} phase is a fine Fe rich precipitation of varying sizes (<0.5 µm in diameter) with plate-like morphology that are distributed throughout the α grains along certain crystallographic directions forming within the α-matrix at 850°C. κ_{III} phase is a fine lamellar "finger-like" eutectoid structure and forms at the boundary of κ_I phase [14], [44], [45], [47], [48].

The mechanical properties of the test samples used for the study are summarised in table 1.

Ultimate tensile strength	Yield strength	Density	Hardness
650 MPa	270 MPa	7.65 g cm^{-3}	160 HB

Table 1: *Mechanical properties of C95800 NAB*

The general corrosion rate of NAB in seawater is considered to be 0.06 mm $year^{-1}$ [13]. The galvanic potentials of NAB in flowing salt water is between -0.1 V to -0.25 V at a velocity of 2.5 to 4 m s^{-1} at a temperature range of 10 °C – 27 °C with reference to saturated calomel half-cell -0.15 V to -0.22 V [49]–[51].

2.2 Experimental procedure

Six samples of as-cast NAB were prepared for the experiments. Each sample had a dimension of 25 mm x 25 mm (± 2 mm) with a thickness of 5 mm (± 0.5 mm). The test sample surfaces facing the cavitation rig were wet polished using 120-,

800-, 1200- and 4000-grit silicon carbide (SiC) abrasive papers, and 6 µm diamond paste. They were then cleaned with distilled water and methanol before blow-drying them. The surfaces away from the sonotrode tip were coated with lacquer for protection against exposure to corrosion. The samples were left inside six individual, clean and uncontaminated plastic bags for a week to ensure the formation of air-formed oxide films. The preparation procedure was repeated for each sample after each test in order to reuse the samples.

The test samples were tested using the experimental conditions and procedure as given in previous work conducted, found in Ref [44] using indirect ultrasonic vibratory transducer operating at a frequency of 19.5 kHz and an amplitude of 80 µm ± 0.2 µm (peak-to-peak). The ultrasonic vibratory apparatus was used for the research as it is the most commonly used device that produces a periodic pressure field, inducing the periodic growth and collapse of a cloud of cavitation bubbles [54]. The ultrasonic vibration mechanism also provides the fastest approach to obtaining cavitation results for a wide range of engineering materials amongst all the various cavitation test methods [55]. The indirect cavitation method was chosen in order to conduct in-situ electrochemical analysis. The time period for each test was 1 h, except the polarization test, in fresh batch of mediums. The standoff distance between the sample and the ultrasonic transducer was kept constant at 2 mm. The temperature and the pH of the water were monitored to remain constant for each test at room temperature of 17 °C ± 0.5 °C and a pH range of 7.5 - 8.5. Figure 1 gives the schematics of the test arrangement.

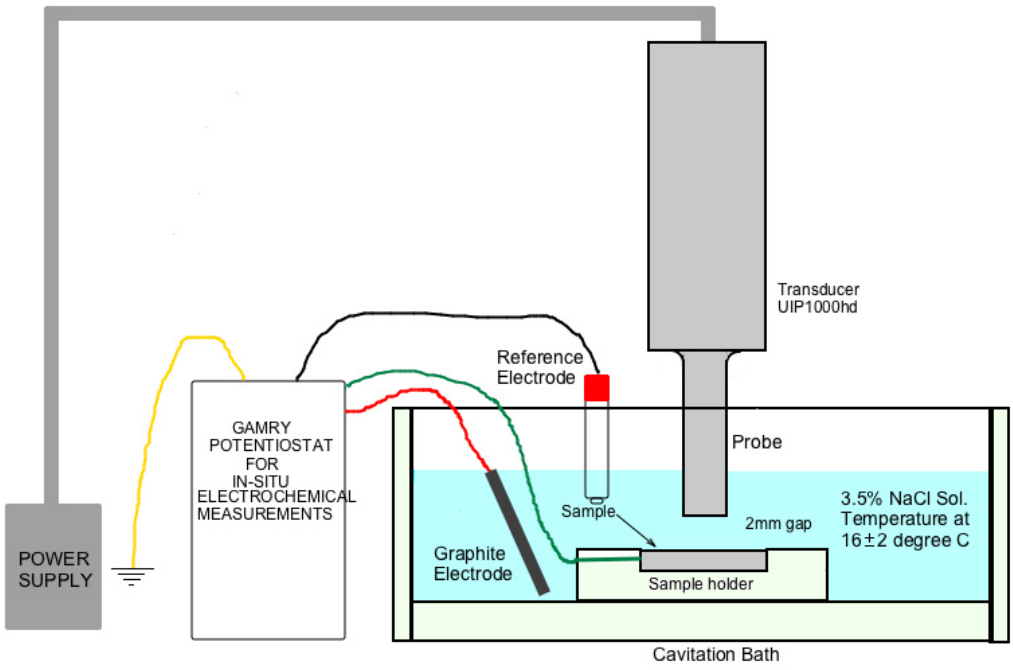

Fig. 1: *Schematics of the cavitation rig with specimen connected to the potentiostat for cavitation erosion-corrosion measurements* [44].

The synergy measurement was obtained using three main approaches, namely the gravimetric mass loss method, the volumetric mass loss method, and mean depth of penetration rate (MDPR) method. Under the gravimetric method, the erosion rates (E) were obtained in two different ways: by erosion in 5 L of distilled water for 1 h, and by subjecting the samples to cavitation erosion in 3.5% NaCl solution with cathodic protection for 1 h. The corrosion rates (C) were also obtained in two different ways, gravimetrically by using mass balance, and from the potentiodynamic polarization curves. Alicona InfiniteFocus 3D non-contact optical profilometer was used to obtain the synergy value using the MDPR method, and the volumetric mass loss method. Alicona was also employed to obtain surface topography and roughness measurements at a vertical resolution of 10 nm – 50 nm.

For the electrochemical tests the samples were kept at OCP using the GAMRY Ref600 potentiostat while their EIS values were monitored. The EIS frequencies used were between 100000 (initial) Hz - 0.1 (final) Hz. The samples were used as the working electrodes, with Ag/AgCl as the reference electrode and graphite rod as the counter electrode. The parameters for conducting the OCP and EIS tests were set and performed in the GAMRY Framework software. The samples were tested under C and T conditions 3 times each. The data obtained were analysed in the GAMRY Echem Analyst software. For the polarization test, two samples were subjected to potentiodynamic polarization scan at a scan rate 0.167 mV s^{-1} under static conditions in 3.5% NaCl solution in order to obtain pure corrosion rate in terms of mass loss by applying Faraday's laws of electrolysis. The potential of -400 mV against silver chloride electrode (Ag/AgCl) was also obtained from the polarization curve for the pure erosion test in 3.5% NaCl solution subjected to cathodic protection.

For the synergy evaluation, five different synergy values were calculated for the samples. Using Equation (1), three tests were conducted for each sample in order to obtain the synergy rates.

- Pure erosion (E): Two different methods were employed for the pure erosion test. Three samples were subjected to erosion performed in 5 L of triple distilled water for 1 h. And three samples were subjected to cavitation erosion in 3.5% NaCl solution with cathodic protection for 1 h.

- Pure corrosion (C): Four samples were subjected to in-situ electrochemical measurements kept at open circuit potential (OCP), and electrochemical impedances spectroscopy (EIS) analysis were conducted in 3.5% NaCl solution for 1 h. Two sample materials were also subjected to potentiodynamic polarization, at a potential range between -1 V to 2 V, to obtain C by applying Faradaic conversion.

- Combined cavitation erosion-corrosion (T): all six samples were cavitated in 5 L of 3.5% NaCl solution for 1 h while subjected to OCP.

The masses of the samples were recorded before and after each experiment with a precision mass balance for gravimetric analyses (± 0.01 mg). Each sample was weighed 5 times, each after recalibration of the balance after every measurement, and an average was considered per test. The samples were analysed for microstructural characterization using JOEL (JSM6500F) scanning electron microscope (SEM) employed for microstructural morphology analysis before and after cavitation at an acceleration voltage of 15.0 kV, a probe current at medium (6 nA – 13 nA), and a working distance of 10 mm and above. For clearer microstructural evaluation backscattered electron imaging was also employed. Samples were also transverse sectioned to observe the subsurface impacts of cavitation on the microstructure. For SEM analysis of the transverse sections, the samples were cut laterally with diamond saw, and then hot-mounted in Bakelite resin mould. The interested surface was then polished using 1200- and 4000- grit SiC abrasive paper before mirror finishing it with 1 and 6 µm diamond paste.

3. Results and discussion

Table 2 gives the chemical composition in weight %, for the alloy as well as the individual phases obtained under EDS.

Micro-structural Phases	Chemical composition in weight %					
	Cu	Si	Al	Mn	Fe	Ni
Alloy	80.25	0.03	8.79	3.56	4.63	5.10
Alpha	85.39	-	7.19	0.87	3.35	3.20
Kappa 1	15.08	1.66	13.29	1.72	57.53	10.72
Kappa 2	17.61	1.52	14.02	1.50	51.90	13.44
Kappa 3	45.15	-	18.76	1.19	10.91	23.99
Kappa 4	3.10	4.01	10.99	2.05	72.80	7.05

Table 2: *Chemical composition of the individual phases in the as-cast NAB (C95800) samples, confirmed under EDS.*

3.1 Surface analysis

Cavitation erosion damage undergoes several periods of activity. To understand the gradual mass loss rate and the erosion behaviour of each materials, the

material erosion wear rate is typically analysed by conducting cavitation on the samples over a period of time, with periodic mass loss measurements at each interval. Hence, the erosion wear rate curve for as-cast NAB sample, represented in Figure 2 shows the cumulative erosion rate, plotted as a function of erosion time, obtained after each exposure by dividing cumulative weight loss by total exposure time.

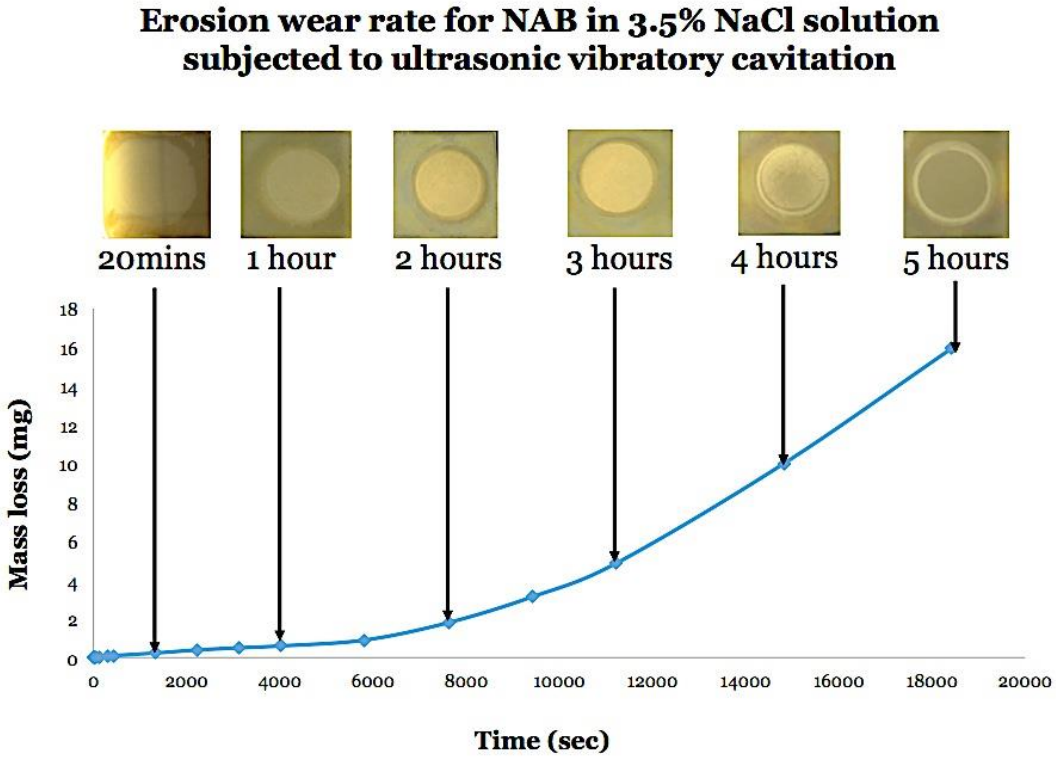

Fig. 2: *Cumulative cavitation erosion rate curve for NAB tested in 3.5% NaCl solution for a time period of 5 h and 14 min.*

Figure 3 shows the optical image of a NAB sample after 1 week of air-formed oxide film formation, with distinct microstructures, before subjecting to cavitation in 3.5% NaCl solution.

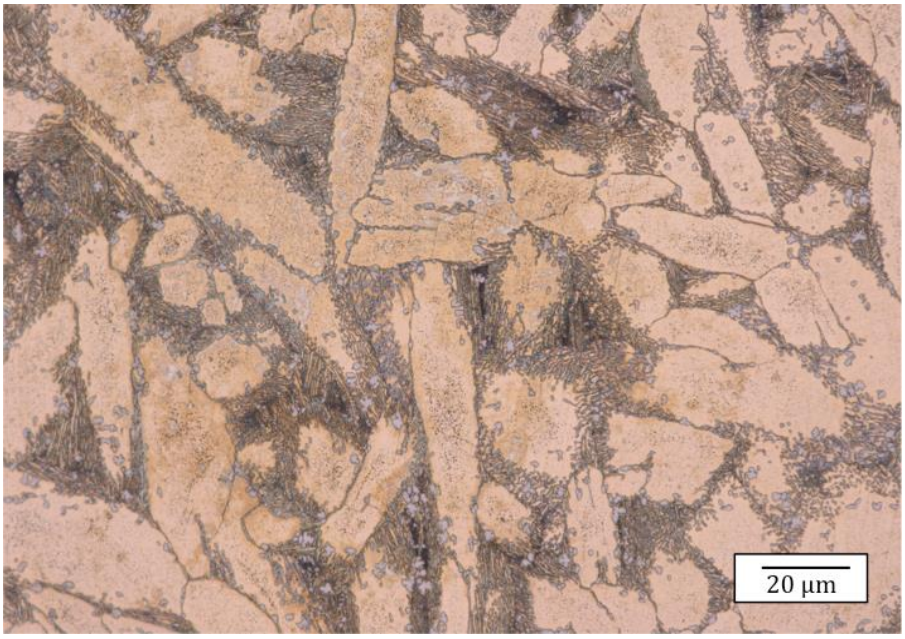

***Fig. 3**: Microstructure of air-formed oxide filmed NAB before cavitation as seen under the optical microscope.*

Figures 4 (a)-(f) show the optical images of air-formed oxide filmed NAB surface under cavitation in 3.5% NaCl solution over time, taken from the centre of the erosion scar. First, the removal of oxide layer from around the phase boundaries was observed (Figure 4 (a)) in the form of light brown oxide layer islands found in the alpha region, after 30 min of cavitation in 3.5% NaCl solution. After 1 h of cavitation, (Figure 4 (b)), the microstructure seemed to undergo cavitation erosion as well as selective phase attack at the phase boundaries.

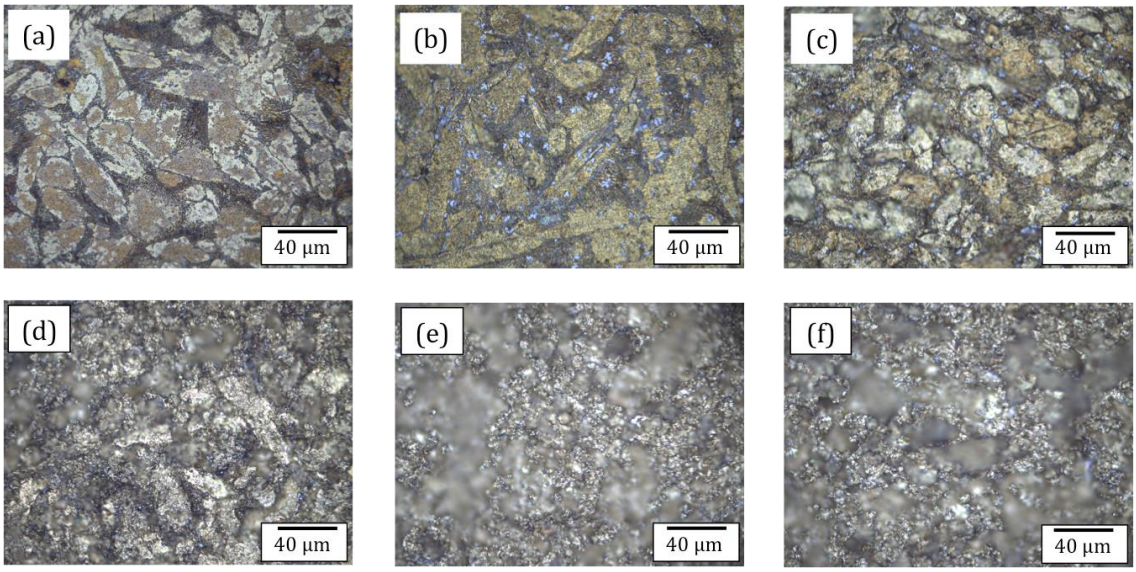

***Fig 5**: Optical images of the progression of cavities on air-formed oxide filmed NAB after cavitation erosion for (a) 30-min, (b) 1 h, (c) 2 h, (d) 3 h, (e) 4 h, and (f) 5 h in 3.5% NaCl solution, showing the increasing roughness of the surface, and growth in cavity sizes with time.*

On further cavitation, the cavities seemed to gradually grow in size from 10-µm (Figure 4 (c)) to up to 80-µm (Figure 4 (f)), while the overall surface roughness also seemed to increase over time after 2, 3, 4 and 5 h of cavitation (Figure 4 (c)-(f)). The number of cavities also increased after 5 h of cavitation, as seen in Figure 4 (f).

The cavitated surface of the test sample appeared to comprise of three easily distinguishable damage regions, formed in concentric rings of cavitated and non-cavitated regions around a centrally damaged area as seen in Figure 5. The surface topography was then obtained by scanning the sample surface laterally across the diameter.

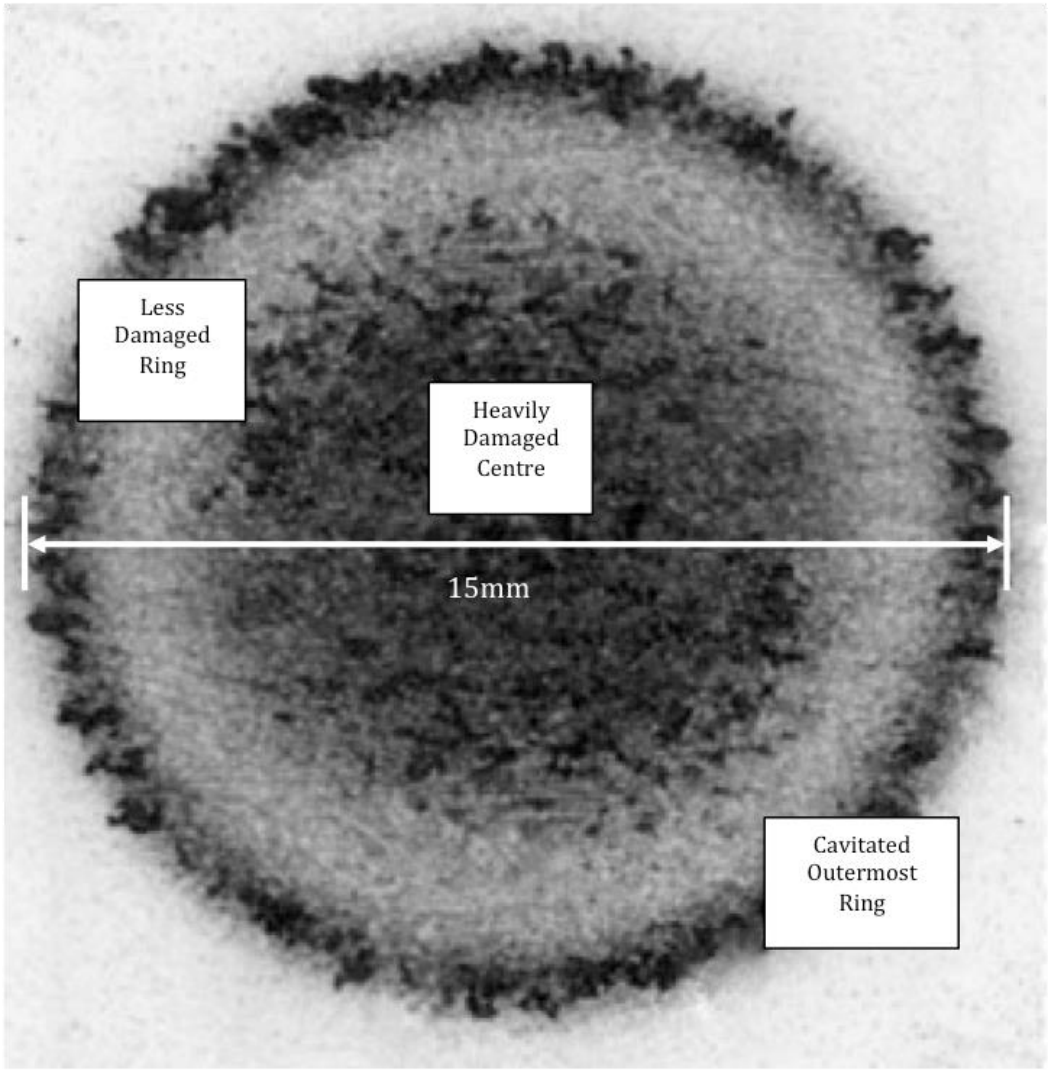

Fig. 5: *Surface profile at the centre of the cavitated surface of NAB after 1 h of test measured in Alicona.*

From the scanned topography profile it was clearly seen that the outer ring undergoes more material loss than the centre with higher surface roughness at the edge of the eroded region. Figures 6 (a) and (b) show the wear profile of air-

formed oxide filmed NAB sample cavitated for 1 h in distilled water, and in 3.5% NaCl solution, respectively.

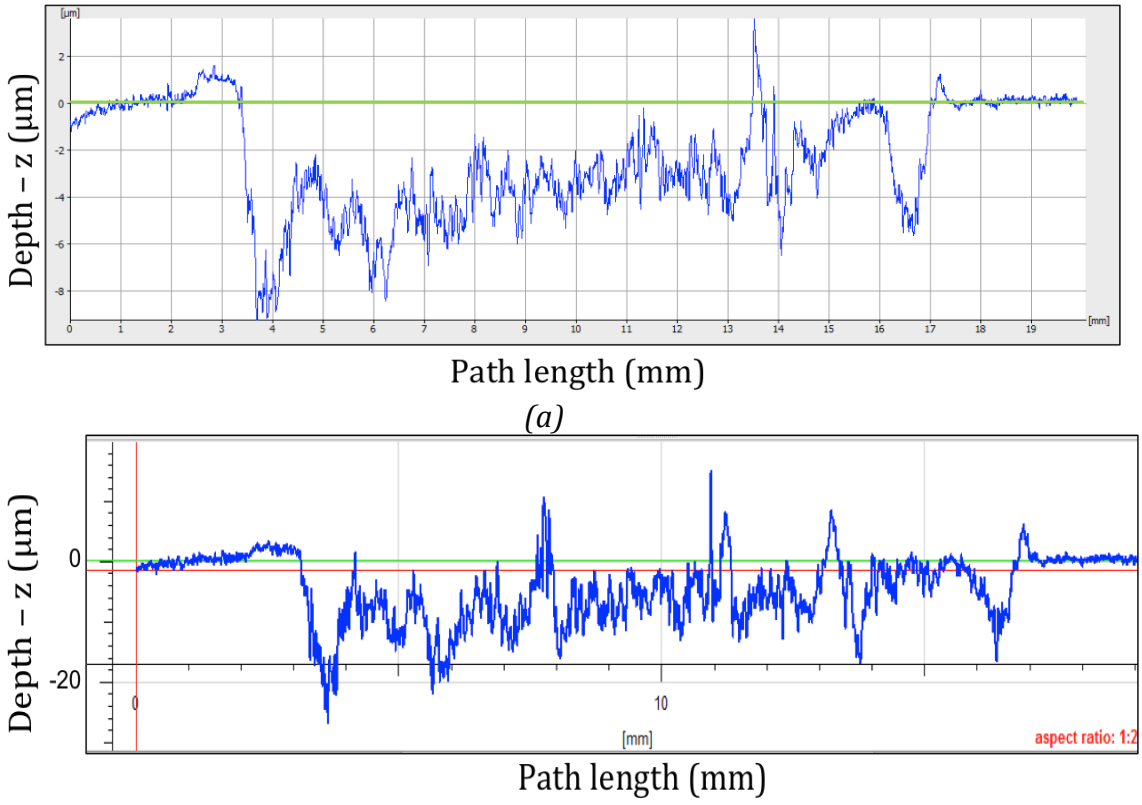

Fig. 6: *Wear scar profile of air-formed oxide filmed NAB after cavitation in (a) distilled water, and (b) in 3.5% NaCl solution for 1 h, obtained using Alicona 3D profilometer.*

The wear profile of the air-formed oxide filmed NAB cavitated in 3.5% NaCl solution (Figure 5 (b)) exhibited much higher erosion profile (almost double), compared to the profile obtained in distilled water (Figure 5 (a)).

After conducting the cavitation tests on the samples, the surface profilometry and R_a, mean depth of penetration (MDP) and the volume loss were measured using both Alicona. Table 2 tabulates the measured values of R_a before cavitation, in distilled water and in 3.5% NaCl solution with and without cathodic protection. Whereas, the MDP and the volume loss were measured for the samples cavitated in distilled water for pure erosion, and the combined erosion-corrosion test in 3.5% NaCl solution.

Average surface roughness, R_a (in µm)				Mean depth of penetration, MDP (in µm)		Measured volume loss (in mm^3)	
Before cavitation	Distilled water	3.5% NaCl sol. With CP	3.5% NaCl sol.	Distilled water	3.5% NaCl sol.	Distilled water	3.5% NaCl sol.
0.063 ± 0.003	0.153 ± 0.003	0.160 ± 0.003	0.165 ± 0.003	0.645 ± 0.003	0.955 ± 0.003	0.115 ± 0.003	0.169 ± 0.003

Table 3: *Average roughness, mean depth of penetration and volume loss measured under pure erosion and combined erosion-corrosion test conditions using Alicona.*

3.2 Microstructural analysis

Figure 7 shows the general microstructural morphology of the as-cast NAB C95800 used for the experimental study, taken under SEM.

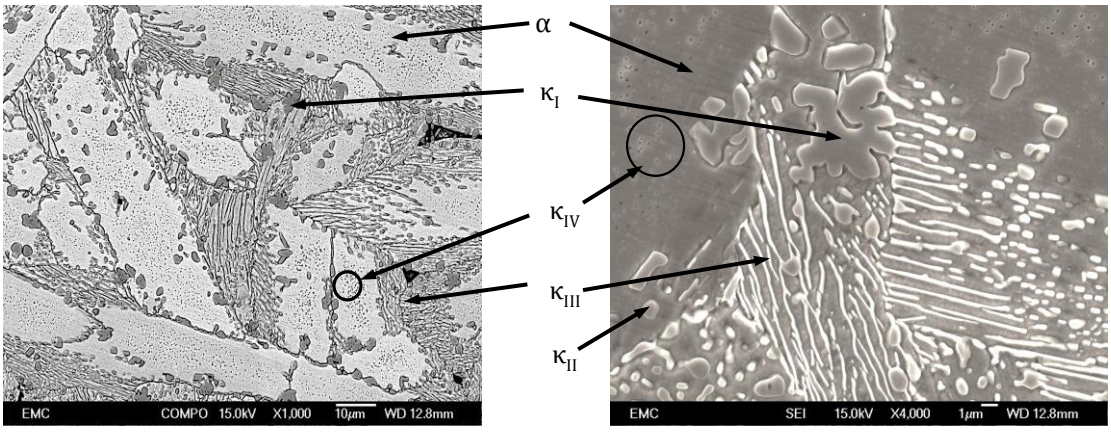

Fig. 7: *Microstructural morphology of as-cast NAB. κ_I is the globular dendritic structure, κ_{III} is the lamellar "finger-like" structure, and κ_{IV} is the very fine particulate imbedded within the α matrix.*

The samples were observed under the SEM for microstructural analysis before and after each test. Figure 8 (a) and (b) show the magnified images of the microstructures of a cavitation-eroded region for NAB tested in distilled water for 1 h. And Figure 8 (c) and (d) depict the microstructures of a cavitation-eroded region for NAB cavitated for 1 h in 3.5% NaCl solution.

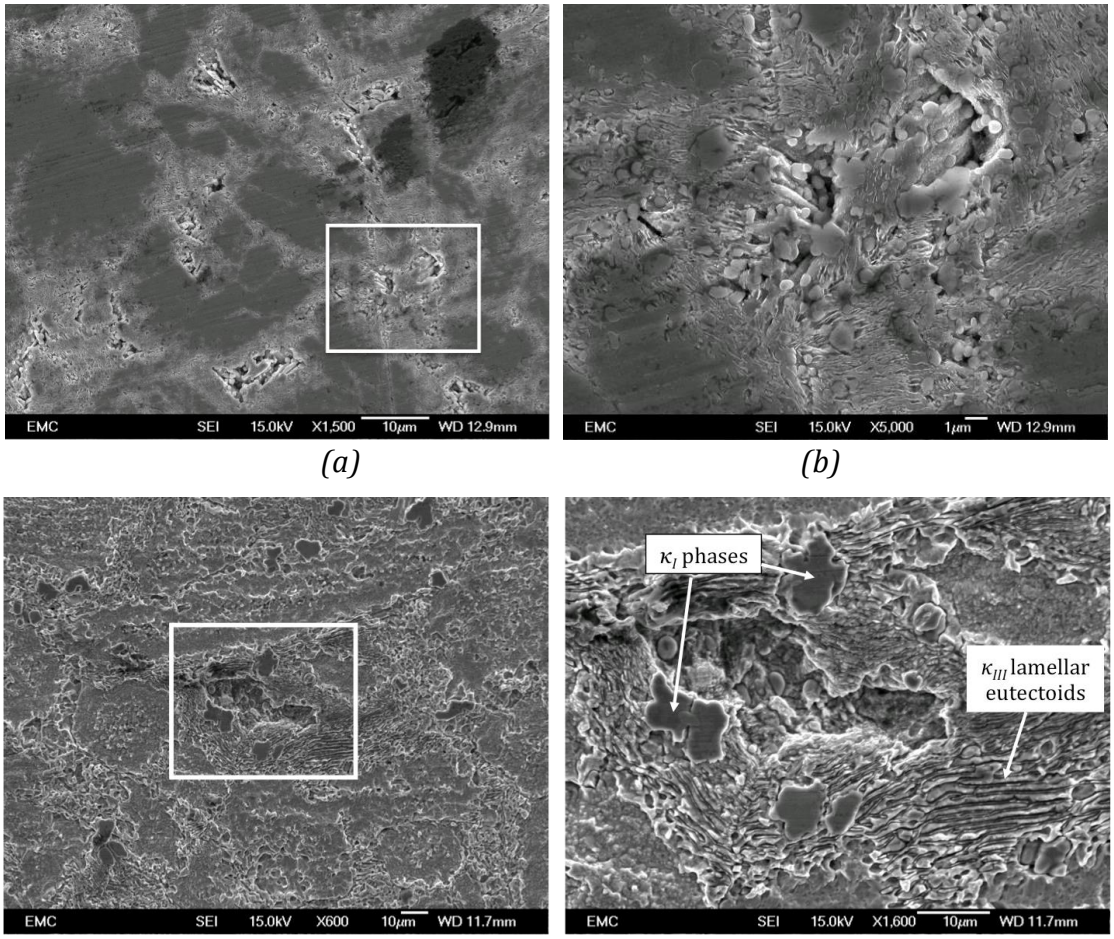

Fig. 8: *SEM compo/backscattered images of (a) small boundary erosion on air-formed filmed NAB in distilled water; (b) shows the magnified image of the cavities of size 10-μm at the selected area in (a); (c) SEM image of a 50-μm large cavity on the sample surface undergone cavitation erosion-corrosion in 3.5% NaCl solution; and (d) the magnified image of a cavity in (c) showing selective phase attack at the α-κ phase boundaries leaving κ_I globules and κ_{III} lamellar phases exposed.*

For the cavitation erosion-corrosion test in distilled water, small cavities of sizes 10 μm – 30 μm were found in the grain boundaries as shown in Figure 8(b). This was considered to be due to the soft *α*-matrix surrounding the hard iron-rich *κ* phases being most vulnerable to cavitation attack. The *κ*-precipitates and precipitate-free *α*-zones did not suffer any visible cavitation after 1 h of cavitation test in distilled water, as also reported in ref [44].

Comparatively, the cavitation erosion-corrosion test in 3.5% NaCl solution exhibited much larger cavities ranging between 50 μm – 80 μm. This again proved that NAB underwent selective phase attack at the *α*-*κ* phase boundaries, although more aggressively than under distilled water, leaving κ_I globules and κ_{III} lamellar phases exposed, Figure 8 (c).

Figure 9 (a) and (b) show the transverse cavitation erosion pattern on the surface after 1 h of testing in distilled water, detailing a cavity formed due to the erosion of the *α*-phase at the *α*-*κ* phase boundary. Enlarged image of the transverse sections of the cavities show cavity growth and crack propagation along the α-κIII phase boundaries (Figure 9 (b)).

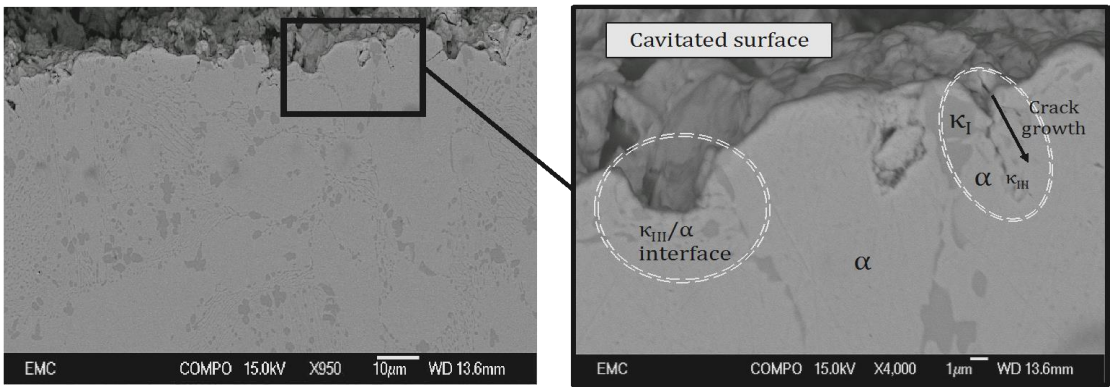

(a) *(b)*

Fig. 9: *SEM images of NAB sample under pure E (distilled water) conditions: (a) transverse-sections of a cavity; (b) detailed magnified image of cavities in (a), exhibiting crack propagation along the α-κ_{III} phase boundaries.*

SEM imaging of the transverse sections of the cavitated NAB surface under 3.5% NaCl solution revealed the selective phase erosion leading to micro-crack propagation into the material across the *α*-*κ* interface. From the SEM results, it can be concluded that the material undergoes enhanced erosion in the presence of corrosion, i.e. ΔE has a higher contribution to the synergistic relation between wear and corrosion.

From the intrinsic microstructural results obtained, it was evident that the microstructural properties of the material, as well as the individual properties of each phase within the microstructure, played very important role in determining the cavitation behaviour of the materials. The sizes on these microstructural phases also played significant role, as it was seen that more the grain boundaries, more the material was vulnerable to boundary erosion and selective phase attacks. Softer phases surrounding the harder intermetallics were seen to undergo erosion more, due to the accumulation of subsurface strain caused by the repetitive hammering of imploding bubbles, and lower fracture toughness of the softer phase.

3.3 Electrochemical analysis

Four samples were subjected to pure corrosion test under OCP, and three samples were subjected to combined erosion-corrosion test kept at OCP. Figure 10 is the OCP curve obtained for NAB in pure corrosion and erosion-corrosion in

3.5% NaCl solution, where V_f is the reference potentials in millivolt. It can be seen NAB reached stability at -210 mV under pure corrosion. For the combined erosion-corrosion tests, the cavitation was applied to the sample kept under OCP after a delay of about 600 s [44].

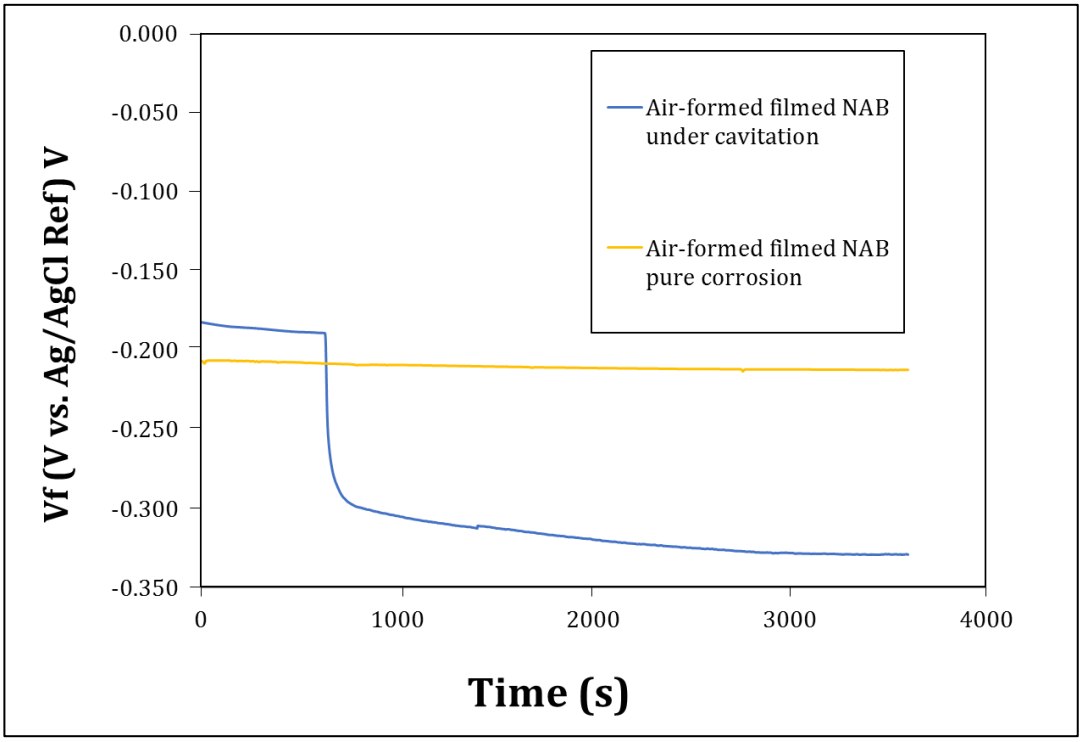

Fig. 10: *OCP for NAB in 3.5% NaCl solution for 1 h with and without cavitation* [44].

It can be seen that under pure corrosion, the measured OCP shift slightly negatively at around -210 mV. This indicates that the thin layer of air-formed protective oxide film on NAB can be slowly broken down due to localized corrosion, causing selective phase attack, during its immersion in the 3.5% NaCl solution. However, there is a dramatic negative shift in OCP upon cavitation impact. As seen from Figure 8, the OCP shifted from -170 mV to about -300 mV upon the application of cavitation, but attained stability within 150 s at a lower potential (of -310 mV). It is noteworthy that under cavitation impact the OCP very gradually shifted towards more negative value with time, meaning gradual depassivation of the surface over time.

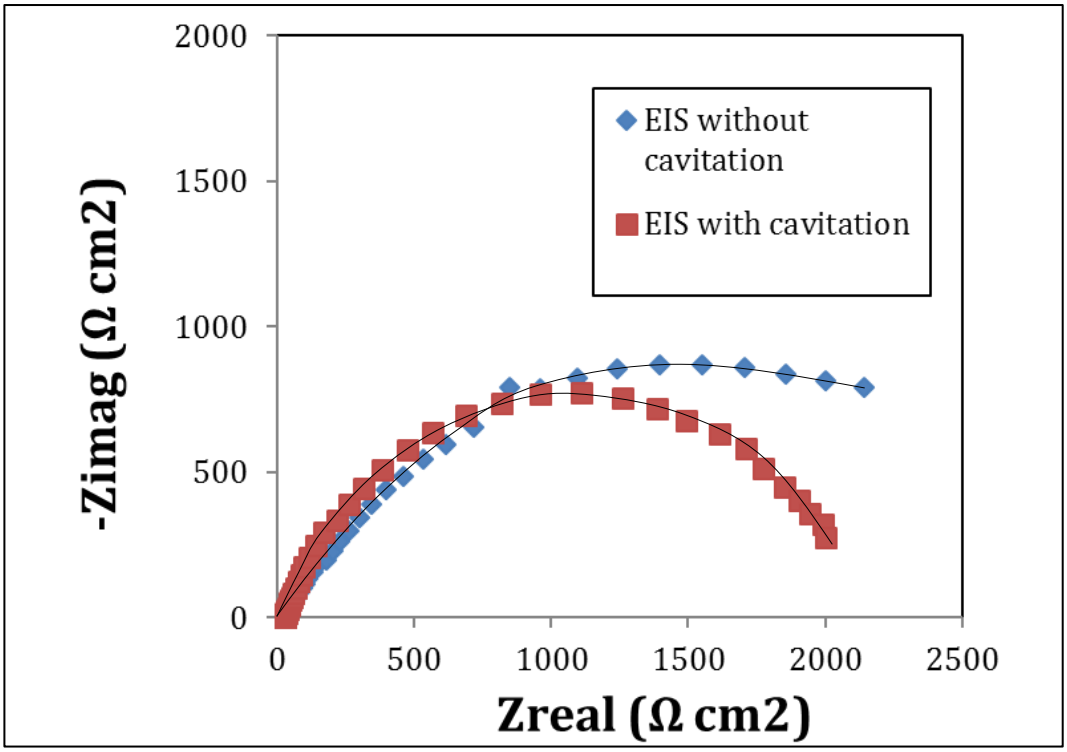

Fig. 11: *Nyquist plots for NAB samples in 3.5% NaCl solution with and without cavitation.*

Figure 11 is the Nyquist curves for the NAB samples undergoing pure corrosion and combined erosion-corrosion test. It can be clearly seen that the material exhibited single time-constant plots with single semi-circles and did not undergo diffusion, either under pure corrosion or cavitation erosion-corrosion tests. The radius of semi-circle is relevant to polarization resistance, where the larger the semicircle is, the higher the polarization resistance. From Figure 12 it can be seen that the polarization resistance is significantly decreased with cavitation with much smaller semicircles, which indicate the polarization resistance.

Figure 12 shows the EIS Bode plots for the NAB samples under pure corrosion and during cavitation. It can be seen that the EIS spectra in both cases exhibit single time-constant behaviour in the investigated frequency range. It was seen that the impedance of NAB under corrosion was slightly lower than that under cavitation erosion-corrosion.

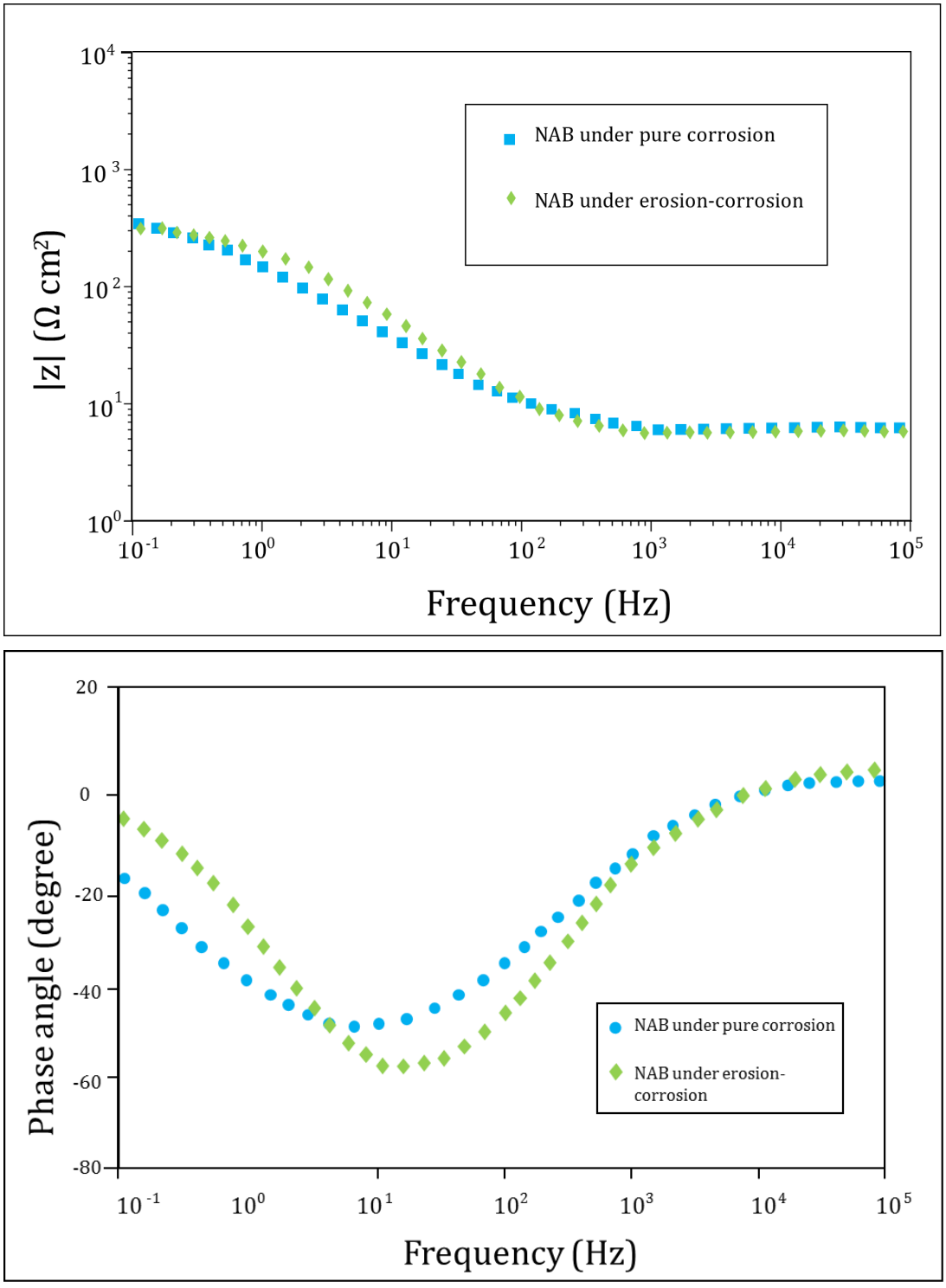

Fig. 12: *EIS Bode curve for NAB in 3.5% NaCl solution under pure corrosion and during 1 h of cavitation.*

The EIS results obtained were also verified using fit models. Fit models or equivalent circuit models are used to model and analyse EIS spectra results that can be built in the GAMRY Instrument Echem Analyst software. The electrochemical cells are simulated in the software by incorporating various factors such as electrode double layer capacitance, electrode kinetics, diffusion

layer and solution resistance. The impedance of the element depends on the element type and the values of the parameters that characterize that element. The protective oxide layer on NAB subjected to cavitation may become porous. These pores could be considered as non-coated portions of substrate. However, due to their small size, the exchange of the electrolyte between the pore and the bulk material may be hampered, therefore, the ion concentration inside the pores could differ from the bulk concentration. This results in an electrolyte resistance R_{pore} different from the bulk electrolyte (solution) resistance, R_s. For NAB, the protective oxide layer is considered to be a mixed Cu/Al oxide, mostly assumed to be Al_2O_3, which is a non-conductive ceramics, hence, considering there is no electron passing through this layer, it is modelled using only one capacitance, C_{pl}. Then the interface between the solution and the material substrate through the pore needs to be considered, hence the model incorporates the resistance of the inner substrate layer, R_{inner}, and the constant phase element, C_{inner}, parallel with R_{inner}.

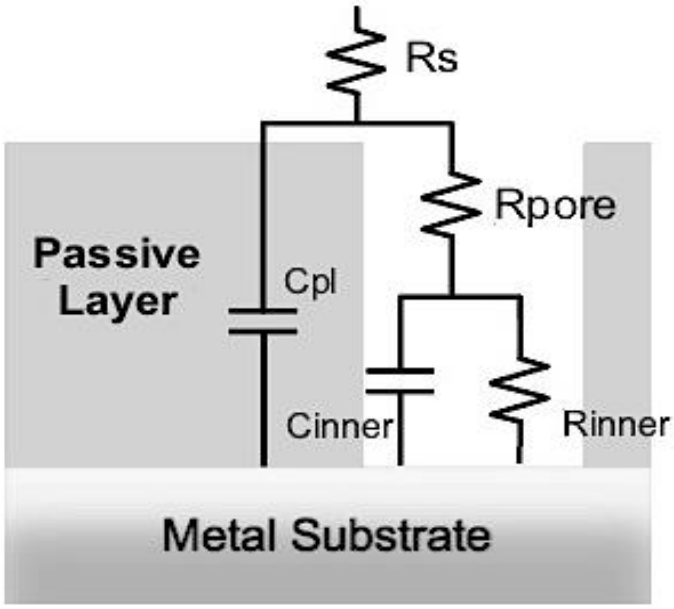

Fig. 13: *A porous non-conductive coating layer with the resulting equivalent circuit.*

Figure 13 gives the respective equivalent circuit that incorporated the pores in the passive layer on the material surface where, R_s is the bulk solution resistance, R_{pore} is the resistance of the pores, C_{pl} is the capacitance of the passive layer, and R_{inner} and C_{inner} are the resistance and constant phase element of the metallic substrate under the passive layer. From the fit model illustrated in Figure 14, the resistance elements at the pores and the inner layer were compared for the results obtained from EIS test for NAB plotted in Figure 12.

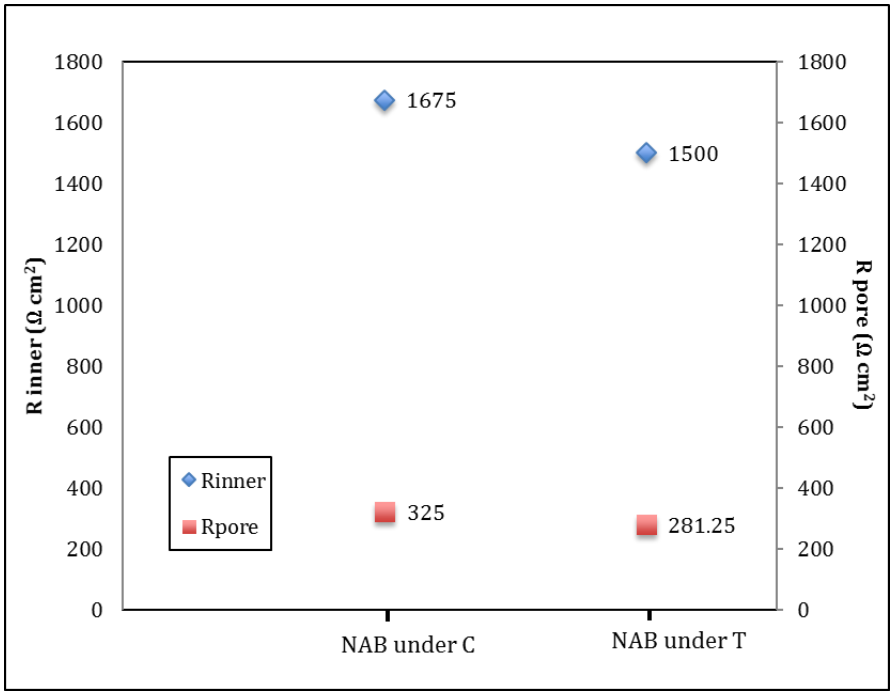

Fig. 14: *EIS fit plot for NAB under C and T conditions.*

From Figure 14 it can be seen that for NAB the substrate resistance (R_{inner}) is higher than the pore resistance (R_{pore}) in both cases. The substrate and pore resistance of NAB subjected to C was higher than that obtained under T. This can be due to an increase in pore sizes or numbers induced under cavitation, enhancing mass transport, causing the decrease in the R_{inner} and the R_{pore} value. However, the values do not differ by a large margin, which could be due to the surface undergoing rapid passivation process even though under the cavitation impact, causing the corrosion process to slow down.

Figure 15 plots the polarization curves for NAB. The potential of -400 mV against silver chloride electrode (Ag/AgCl) was also obtained from the polarization curve for the pure erosion test in 3.5% NaCl solution subjected to cathodic protection.

The sample materials were expected to undergo rapid redox reactions as shown from Equations (3) - (6) taking place in the electrochemical cell [16].

Anodic reaction:

$Cu + Cl^- \rightarrow CuCl + e^-$ ...(3)

$Cu + 2Cl^- \rightarrow CuCl_2^- + e^-$ ...(4)

And cathodic reaction:

$Cl^- + H^{+-} \rightarrow HCl$ ...(5)

$O_2 + 2H_2O + 4e^- \rightarrow 4OH^-$ ...(6)

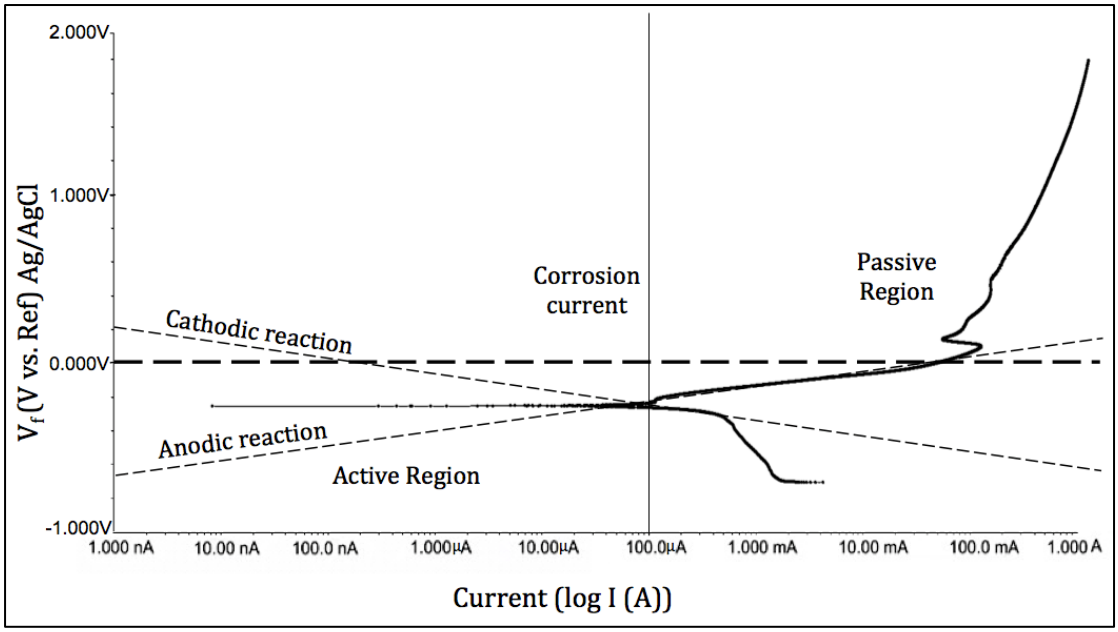

Fig. 15: *Polarization curve for the NAB in 3.5% NaCl solution showing Tafel extrapolation of corrosion current.*

From the polarization results the corrosion current density (I_{corr}) was found to be at 16.0 µA cm^{-2} using Tafel extrapolation. From the I_{corr} value the mass loss rate of the sample was calculated using Faradaic conversion, given by Equation (7).

$$\text{Mass loss rate} = \frac{I_{corr} \times \text{Atomic mass of corroding element} \times \text{exposed area}}{\text{number of electrons freed} \times \text{Faraday's constant}} \quad \ldots(7)$$

Where, the rate of mass loss is in mg cm^{-2} h^{-1}, and
Faraday's constant = 96485 C mol^{-1}

From Equations (3) and (4), the corroding element was considered to be copper, and the number of free electrons (n) was considered 1 and 2. Hence, the mass loss values obtained for pure corrosion using the potentiodynamic polarization technique were found to be 0.382 mg ± 0.002 mg for n = 1, and 0.197 mg ± 0.002 mg for n = 2.

3.4 Synergy evaluation

Using Equation (1), the synergy was calculated using five different methods. The first method used mass loss as the parameter for synergy. The second and third methods employed Alicona to obtain the volumetric mass loss and the mean depth of penetration rate from Table 2 as the parameters for measuring synergy, all obtained in distilled water as the medium for pure erosion.

The pure erosion test was also conducted in 5 L of 3.5% NaCl solution while subjecting the samples to cathodic protection as the fourth method. It must be noted that the pure corrosion test provided a negative value for the synergy calculation due to a gain in mass observed gravimetrically after each test. Due to this the results were rather dispersive and hence, the fifth method employed polarization technique to obtain C. Table 4 tabulates the measured synergy values for NAB for each test, obtained using the five different methods to estimate the synergy between cavitation erosion and corrosion.

Method Used	**T (mg)**	**E (mg)**	**C (mg)**	**S=T-(E+C) (mg)** Using Equation (1)	**(S/T) x100**
MDPR (μm h^{-1}) *(Measured by Alicona)*	0.955 ± 0.003	0.645 ± 0.005 (in distilled water)	0.000 ± 0.002	0.310 ± 0.010	32%
Volumetric Mass Loss (mg) *(Measured by Alicona)*	1.29 ± 0.05	0.88 ± 0.04 (in distilled water)	0.00 ± 0.02	0.41 ± 0.11	31%
Gravimetric mass loss (mg) *(Measured by mass balance)*	1.48 ± 0.02	1.00 ± 0.05 (in distilled water)	-0.61 ± 0.04	1.09 ± 0.11	73%
Gravimetric mass loss (mg) *(Measured by mass balance)*	1.48 ± 0.02	1.52 ± 0.05 (with cathodic protection)	-0.61 ± 0.04	0.57 ± 0.11	38%
Gravimetric mass loss (mg) *(T and E measured by mass balance, C calculated by Equation 7)*	1.48 ± 0.02	1.00 ± 0.05 (in distilled water)	0.197 ± 0.002 For n = 2;	0.28 ± 0.072	19%
			0.394 ± 0.002 For n =1 (Polarization and Faradaic conversion)	0.098 ± 0.072	6%

Table 4: *Synergism summary for NAB obtained using five different test methods.*

The highest synergy measured from the 5 different methods (tabulated in Table 4) was found to be 73% under gravimetric method (method 3) while the lowest resulted from method 5 with E conducted for 1 h in 5 L of distilled water. This yielded 6 - 19% synergy when a polarization method was used for C. The gravimetric results measured using the cathodic protection method for E was found to give a synergy of 38%. As for the results obtained via Alicona, the synergy was found to be 31% using the volumetric mass loss method, and 32% using MDPR method. The value of E was higher than C in every method. The values of T were higher than E, except for the cathodic protection method. From the results, it can be inferred that corrosion tends to enhance mass loss, except in the case where cathodic protection was used to determine E, where corrosion appeared to have a negative effect on total mass loss.

From Table 4 it can be seen that distilled water exhibited lower mass loss when compared to cathodic protection test. On analysing under the SEM, it was observed that under cathodic protection the number of cavities had actually increased, which has also been reported in the literature [14], [15]. Hence, there was an increase in the mass loss observed when applying cathodic protection, although the grain-boundary attack was lower than that found in distilled water. This gives an interesting result showing that using distilled water reduces mass loss by about 0.5 mg relative to the CP technique, giving almost double the synergy obtained under other two conditions.

The best method for S quantification is probably method 5 where gravimetric measurements are used for E and T (E from distilled water experiments) and C is from polarization and Faraday conversion techniques. However, it is uncertainty on the value of n for Faradaic conversion and thus only a range of S% can be given.

In a study by Kwok, Cheng and Man [22], the synergistic effect of cavitation erosion and corrosion of copper-based alloys and bronze, among many other engineering alloys using an 20 kHz ultrasonic vibrating cavitation at a peak-to-peak amplitude of 30 μm in distilled water and in 3.5% NaCl solution at 23 °C was investigated. It was found that synergism had a significant effect on the mass loss with it contributing up to 85% total damage. They calculated the synergy via mean depth of penetration rate method and concluded that the Cu-based alloys had a synergy percentage of 2.7 - 4.5% with 95 – 97% of the total damage attributed to pure erosion only. It was also found that corrosion only played a minor role of about 0.1–1.8% in the overall cavitation erosion–corrosion for copper-based alloys. They also performed several experiments on laser treated metals such as austenitic steel alloy and NiCrSiB-1050-2 alloy in 3.5% NaCl solution [56].

In the studies conducted by Wood and Fry [25], they investigated the fundamental mechanisms of the synergistic effect of cavitation erosion and corrosion for copper and cupro-nickel alloys in seawater. The test was conducted in an all-plastic cavitation tunnel comprising of a 60° symmetrical wedge cavitation source. The specimens of 10 mm × 20 mm working section were held under potentiostatic control in a flowing seawater system at an upstream flow velocity of 14.7 m s^{-1}. The synergy was measured using the depth of penetration method, tested for 4.5 h. They found that that the synergistic effect was most marked when the cavitation erosion occurred in the presence of mild corrosion with 50 - 70% of the damage caused due to pure erosion only. However, corrosion was responsible for 50% of the overall penetration depth. The synergy was found to range between 10 – 29% at different over-potentials of 5 mV – 100 mV for copper, and between 30 – 50% for Cu-Ni alloys. Their preliminary results also suggested that depth of penetration measurements gave clearer indication of the level of synergistic effect compared to mass loss measurements with the majority of the depth of penetration being caused by synergistic mechanisms.

Wood and Hutton [57] plotted the ratio of the synergistic wear to corrosive wear (S/C) against the ratio of erosive wear to corrosive wear (E/C). These tests were conducted using hydrodynamic cavitation, slurry impingement with aqueous slurries containing 2% silica sand particles, and vibratory cavitation for various steels and cast iron in a slurry pot, copper and curpo-nickel alloys, in various corrosive and non-corrosive solutions. These were obtained from the results published in literature [57], as summarized in Table 5.

Point no.	Material	Ref.	Point no.	Material	Ref.	Point no.	Material	Ref.
1	A514	[36]	15	MS1020	[58]	29	Cu	[25]
2	SS-316	[36]	16	MS1020	[58]	30	Cu	[25]
3	SS-316	[36]	17	MS1020	[58]	31	Cu	[25]
4	REM 500	[36]	18	SS-304	[58]	32	Cu	[25]
5	REM 500	[36]	19	SS-304	[58]	33	Cu	[59]
6	A514	[36]	20	SS-304	[58]	34	MS1020	[60]
7	SS-316	[36]	21	Cu	[25]	35	Fe	[61]
8	SS-316	[36]	22	Cu	[25]	36	Fe	[62]
9	REM 500	[36]	23	Cu	[25]	37	Fe	[62]
10	REM 500	[36]	24	Cu	[25]	38	Fe	[62]
11	Cu	[59]	25	Cu	[25]	39	Fe	[62]
12	Cu	[59]	26	Cu	[25]	40	Fe	[62]
13	Cu	[59]	27	Cu	[25]			
14	G cast Fe	[35]	28	Cu	[25]			

Table 5: *Data used for S/C vs. E/C map (as plotted in Figure 16) and their corresponding references* [57], [63] *.*

The S/C and E/C values for air-formed NAB from the current study were also calculated and tabulated in Table 6, and plotted in the graph using the synergy calculation in Table 4.

Material	S/C	E/C
NAB with air-formed film (n=1)	0.20	2.54
NAB with air-formed film (n =2)	1.42	5.07

Table 6: *S/C and E/C values calculated for air-formed oxide-filmed NAB samples using gravimetric method for E measurement, and polarization and Faradaic conversion for C measurement.*

Figure 16 illustrates the linear relationships between S/C vs. E/C plot along with the current results from the NAB. The numbers designated to the points are used to identify the type of materials and the experimental conditions they were subjected to. The solid line represents the materials having medium S/C values (i.e. up to 30% of total wear is affected by synergy); whereas, materials having high S/C values (i.e. more than 60% of total wear is affected by synergy) are represented by the broken line. Points below the solid line were considered as low S/C values, with less than 10% of total wear affected by synergy. And for E/C values above 50, the points could not be distinguished between high and low S/C values. Also, it can be seen that data from this paper for NAB (with air-formed oxide film) lies on the medium S/C value [57], [63].

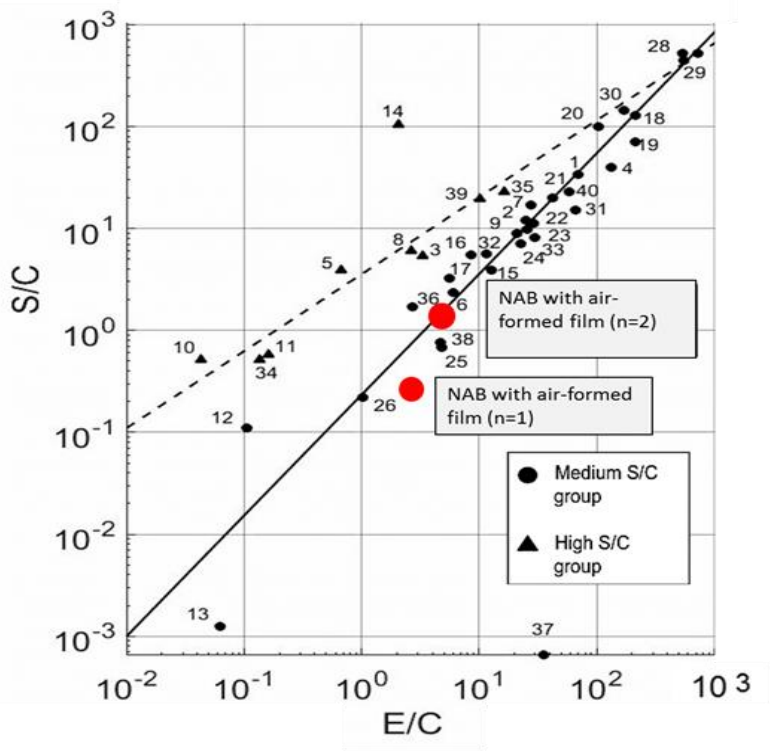

Fig 16: *S/C vs E/C curve* [57], [63].

3.5 Limitations of the methods used

As presented by the author [44], the gravimetric mass loss results were considered more reliable. This is because, although both gravimetric as well as volumetric mass loss measurements are useful and efficient in their own account, they both have major shortcomings.

On one hand, while the data obtained by precision mass balance are generally considered accurate up to 0.01 mg, several factors may affect these results. Water-retention due to absorption via porous layers/coats or selective phase attack may occur that make actuate mass loss measurements difficult. On the other hand, the volumetric analyses can be equally crude since the highest magnification achievable using Alicona is 1000x. It can suffer from loss of data for very smooth and reflective surfaces, or due to re-entrant topography of the surface. Also, in the case where there are sediments, corrosion products, micro-scratches, and burrs existing on the sample surface, it may not clearly differentiate these to allow selective volume loss measurement. This again causes deviation from the true result. Hence, S/T % obtained using gravimetric method for E and T, and polarization technique for C was considered more preferable.

From the study, it must be noted that the errors for E, C and T all sum up while quantifying S, which can lead to significant errors. Given the variables in the synergy results under each test conditions, and also the high error accumulation, the exact value of S is difficult to evaluate. Additionally, an important factor often overlooked, and needs to be realized, is the percentage error for the S/T % values obtained under each individual method. Often, the S values and the corresponding S/T % are quoted in literature without the error bars. However, as seen from the results, these error % values are not negligible, making the S and S/T values less reliable than assumed. Furthermore, it is difficult to resolve S into the separate ΔE and ΔC components. Also, the ΔC component of S is further difficult to measure directly using electrochemical techniques due to the rapid and aggressive nature of the cavitation clouds produced in the experimental set up, affecting the IR drop. In the light of all the results obtained, there is still much left to be answered in the realms of electrochemistry, and the individual contributions of ΔE and ΔC.

4. Conclusion

From the experiments conducted it was concluded that:

- The synergy was calculated using five different methods, involving gravimetric mass loss, measured using a precision mass balance for the samples eroded under both distilled water, and 3.5% NaCl solution while under cathodic protection using GAMRY Potentiostat. Volumetric mass loss and MDPR both employed Alicona non-contact profilometry measurements. The C measurements were obtained using polarization and Faraday conversion methods.

- Synergy was found to be 31% using the volumetric mass loss method, 32% using MDPR method, 74% using gravimetric mass loss in distilled water, 38% using the cathodic protection method, and 31% using the Faraday conversion technique.
- Due to a mass gain observed for C under the OCP method, the result obtained via the polarization technique was considered more realistic and reliable, which gives 6-19% synergism. This range was due to the uncertainty of the exact electrochemical reactions occurring and the number of electrons being transferred. Further studies are needed to elucidate the exact reactions occurring over extended immersion periods.
- Under cathodic protection the number of cavities increased, giving higher mass loss through pitting than that under distilled water, however the grain-boundary attack was lower than that in distilled water.
- The soft α-matrix surrounding the hard κ-phases seemed most vulnerable to cavitation attack, under both E and T conditions.
- NAB was found to be susceptible to prominent selective phase attack of the α-κ phase interfaces in the microstructure in the presence of corrosive environment.

Acknowledgments

The author would like to thank Lloyd's Register for funding the work.

References

[1] N. K. Bourne and J. E. Field, "A high-speed photographic study of cavitation damage," *J. Appl. Phys.*, vol. 78, no. 7, pp. 4423–4427, 1995.

[2] Y. Tomita and A. Shima, "On the Behavior of a Spherical Bubble and the Impulse Pressure in a Viscous Compressible Liquid," *JSME*, vol. 20, pp. 1027–1035, 1977.

[3] J. P. Ghose and R. P. Gokarn, "Propeller Materials," in *Basic Ship Propulsion*, Kharagpur: Allied Publishers, 2004, pp. 166–173.

[4] E. C. Fitch, "Cavitation Wear In Hydraulic Systems," *Machinery Lubrication*, 2011. [Online]. Available: http://www.machinerylubrication.com/Articles/Print/380. [Accessed: 15-Aug-2013].

[5] W. Lauterborn and C. Ohl, "Cavitation bubble dynamics," *Ultrason. Sonochem.*, vol. 4, pp. 65–75, 1997.

[6] C.-D. Ohl, T. Kurz, R. Geisler, O. Lindau, and W. Lauterborn, "Bubble dynamics, shock waves and sonoluminescence," *Philos. Trans. R. Soc. A Math. Phys. Eng. Sci.*, vol. 357, no. 1751, pp. 269–294, Feb. 1999.

[7] Y. Zheng, S. Luo, and W. Ke, "Effect of passivity on electrochemical

corrosion behavior of alloys during cavitation in aqueous solutions," *Wear*, vol. 262, no. 11–12, pp. 1308–1314, May 2007.

[8] G. E. Totten, D. K. Wills, and D. G. Feldmann, Eds., *Hydraulic Failure Analysis: Fluids, Components, and System Effects, Issue 1339*, 1st ed., vol. 3. Philadelphia: ASTM International, 2001.

[9] Y. Zhou and F. G. Hammitt, "Cavitation erosion incubation period," *Wear*, vol. 86, no. 86, pp. 299–313, 1983.

[10] F. G. Hammitt, *Cavitation and multiphase flow phenomena*. McGraw-Hill Book Co., 1980.

[11] "Cavitation in Control Valves," *Samson*. Samson, Frankfurt, pp. 1–62, 2003.

[12] R. Francis, "Bimetallic Corrosion," 1982.

[13] H. S. Cambell, "Aluminium bronze alloys - corrosion resistance guide," no. 80. Copper Development Association, p. 30, 1981.

[14] A. Al-Hashem and W. Riad, "The role of microstructure of nickel–aluminium–bronze alloy on its cavitation corrosion behavior in natural seawater," *Mater. Charact.*, vol. 48, no. 1, pp. 37–41, Feb. 2002.

[15] A. Al-Hashem, P. G. Caceres, W. T. Riad, and H. M. Shalaby, "Cavitation Corrosion Behavior of Cast Nickel-Aluminum Bronze in Seawater," *Corrosion*, vol. 51, no. 5, pp. 331–342, May 1995.

[16] J. A. Wharton and K. R. Stokes, "The influence of nickel–aluminium bronze microstructure and crevice solution on the initiation of crevice corrosion," *Electrochim. Acta*, vol. 53, no. 5, pp. 2463–2473, 2008.

[17] H. M. Shalaby, A. Al-Hashem, H. Al-Mazeedi, and A. Abdullah, "Field and laboratory study of cavitation corrosion of nickel aluminium bronze in sea water," *Br. Corros. J.*, vol. 30, no. 1, pp. 63–70, 1995.

[18] C. T. Kwok, H. C. Man, and F. T. Cheng, "Cavitation erosion and damage mechanisms of alloys with duplex structures," *Mater. Sci. Eng. A*, vol. 242, no. 1–2, pp. 108–120, Feb. 1998.

[19] C. T. Kwok, H. C. Man, and F. T. Cheng, "Cavitation erosion of duplex and super duplex stainless steels," *Scr. Mater.*, vol. 39, no. 9, pp. 1229–1236, Oct. 1998.

[20] C. T. Kwok, H. C. Man, and L. K. Leung, "Effect of temperature, pH and sulphide on the cavitation erosion behaviour of super duplex stainless steel," *Wear*, vol. 211, no. 1, pp. 84–93, Oct. 1997.

[21] S. Z. Luo, Y. G. Zheng, M. C. Li, Z. M. Yao, and W. Ke, "Effect of Cavitation on Corrosion Behavior of 20SiMn Low-Alloy Steel in 3% Sodium Chloride Solution," *Corrosion*, vol. 59, no. 7, pp. 597–605, Jul. 2003.

[22] C. T. Kwok, F. T. Cheng, and H. C. Man, "Synergistic effect of cavitation erosion and corrosion of various engineering alloys in 3.5% NaCl solution," *Mater. Sci. Eng. A*, vol. 290, no. 1–2, pp. 145–154, Oct. 2000.

[23] H. Yu, Y. G. Zheng, and Z. M. Yao, "The cavitation erosion and erosion-

corrosion behavior of carbon steel in simulating solutions of three rivers of China," *Mater. Corros.*, vol. 57, no. 9, pp. 705–714, Sep. 2006.

[24] A. Sakamoto, H. Funaki, and M. Matsumura, "Seminar influence of galvanic macro-cell corrosion on the cavitation erosion durability," *Int. cavitation Eros. test Semin.*, 2000.

[25] R. J. K. Wood and S. A. Fry, "The Synergistic Effect of Cavitation Erosion and Corrosion for Copper and Cupro-Nickel in Seawater," *J. Fluids Eng.*, vol. 111, no. 3, pp. 271–277, 1990.

[26] R. J. K. Wood, "Erosion–corrosion interactions and their effect on marine and offshore materials," *Wear*, vol. 261, no. 9, pp. 1012–1023, Nov. 2006.

[27] K. Darowicki and J. Ryl, "Cavitation erosion , influence of electrochemical corrosion on cavitation – a review," 2011.

[28] Y. Zheng, Z. Yao, X. Wei, and W. Ke, "The synergistic effect between erosion and corrosion in acidic slurry medium," *Wear*, vol. 186–187, pp. 555–561, Aug. 1995.

[29] Q.-Y. Wang, S.-L. Bai, and Z.-D. Liu, "Study on Cavitation Erosion–Corrosion Behavior of Mild Steel under Synergistic Vibration Generated by Ultrasonic Excitation," *Tribol. Trans.*, vol. 57, no. 4, pp. 603–612, Jun. 2014.

[30] R. Malka, D. A. Gulino, and M. Technology, "Erosion corrosion and synergistic effects in disturbed liquid-particle flow," *Corros. Nacexpo*, no. 6594, 2006.

[31] "ASTM G119 - 16 Standard Guide for Determining Synergism Between Wear and Corrosion," *ASTM international*, 2016. [Online]. Available: http://www.astm.org/cgi-bin/resolver.cgi?G119-09(2016). [Accessed: 07-Jun-2014].

[32] B. Vyas and I. L. H. Hansson, "The cavitation erosion-corrosion of stainless steel," *Corros. Sci.*, vol. 30, no. 8, pp. 761–770, 1990.

[33] M. Matsumura, "Erosion-Corrosion of Metallic Materials in Slurries," *Corros. Rev.*, vol. 12, no. 3–4, p. 321, 1994.

[34] J. O. Bello, R. J. K. Wood, and J. a. Wharton, "Synergistic effects of micro-abrasion–corrosion of UNS S30403, S31603 and S32760 stainless steels," *Wear*, vol. 263, no. 1–6, pp. 149–159, Sep. 2007.

[35] W. J. Tomlinson and M. G. Talks, "Erosion and corrosion of cast iron under cavitation conditions," *Tribol. Int.*, vol. 24, p. 67, 1991.

[36] B. W. Madsen, "Measurement of erosion-corrosion synergism with a slurry wear test apparatus," *Wear*, vol. 123, no. 2, pp. 127–142, 1988.

[37] FanAiming, LongJiming, and TaoZiyun, "An investigation of the corrosive wear of stainless steels in aqueous slurries," *Wear*, vol. 193, no. 1, pp. 73–77, 1996.

[38] Y. Li, G. T. Burstein, and I. M. Hutchings, "Influence of environmental composition and electrochemical potential on the slurry erosion-corrosion of aluminium," *Wear*, vol. 181–183, no. Part 1, pp. 70–79, 1995.

[39] S. Zhou, M. M. Stack, and R. C. Newman, “Characterization of Synergistic Effects Between Erosion and Corrosion in an Aqueous Environment Using Electrochemical Techniques,” *CORROSION*, vol. 52, no. 12, pp. 934–946, 1996.

[40] M. M. Stack and B. D. Jana, “Modelling particulate erosion–corrosion in aqueous slurries: some views on the construction of erosion–corrosion maps for a range of pure metals,” *Wear*, vol. 256, no. 9–10, pp. 986–1004, May 2004.

[41] M. M. Stack, N. Corlett, and S. Zhou, “A methodology for the construction of the erosion-corrosion map in aqueous environments,” *WEAR*, vol. 203, pp. 474–488, 1997.

[42] D. a. Shifler, “Understanding material interactions in marine environments to promote extended structural life,” *Corros. Sci.*, vol. 47, no. 10, pp. 2335–2352, Oct. 2005.

[43] A. Neville, T. Hodgkiess, and J. T. Dallas, “A study of the erosion-corrosion behaviour of engineering steels for marine pumping applications,” *Wear*, vol. 186–187, pp. 497–507, Aug. 1995.

[44] J. Basumatary, M. Nie, and R. J. K. Wood, “The Synergistic Effects of Cavitation Erosion–Corrosion in Ship Propeller Materials,” *J. Bio- Tribo-Corrosion*, vol. 1, no. 2, p. 12, Mar. 2015.

[45] E. A. Culpan and G. Rose, “Microstructural characterization of cast nickel aluminium bronze,” *J. Mater. Sci.*, vol. 13, no. 8, pp. 1647–1657, Aug. 1978.

[46] A. Jahanafrooz, E. Hasan, G. W. Lorimer, and N. Ridley, “Microstructural Development in Complex Nickel-Aluminum Bronzes,” *Metall. Trans.*, vol. 14, no. October, pp. 1951–1956, 1983.

[47] F. Hasan, J. Iqbal, and N. Ridley, “Microstructure of as-cast aluminium bronze containing iron,” *Mater. Sci. Technol.*, vol. 1, no. 4, pp. 312–315, 1985.

[48] K. B. Faires, “Characterization Of Microstructure And Microtexture In Longitudinal Sections From Friction Stir Processed Nickel-Aluminum Bronze,” North Carolina State University, 2003.

[49] “Corrosion: Galvanic Corrosion,” *Specialty Steel Industry of North America*. [Online]. Available: http://www.ssina.com/corrosion/galvanic.html. [Accessed: 12-Sep-2013].

[50] F. King, “Corrosion Resistance of Austenitic and Duplex Stainless Steels in Environments Related to UK Geological Disposal A Report to NDA RWMD,” Cumbria, 2009.

[51] J. H. Horwath, “Why Nickel Aluminum bronze for sea water pumps,” *Ampco Pumps Company*, 2002. [Online]. Available: http://www.ampcopumps.com/media/1881/Why_NiAlBz_For_Saltwater.pdf.

[52] H. Meigh, “Cast and Wrought Aluminium Bronzes: Properties, Processes and Structure,” *Inst. Mater. 1 Carlt. House Terrace, London, SW 1 Y 5 DB, UK,*

2000. 404, 2000.

[53] A. Daroonparvar, M. R. Atabaki, Mazar, M. Vakilipour, "Effect of pre-heat treatment on corrosion behaviour of nickel-aluminium bronze alloy," *Assoc. Metall. Eng. Serbia*, vol. 17, no. 4, pp. 183–198, 2011.

[54] R. W. Johnson, *The Handbook of Fluid Dynamics*. Boca Raton: Springer, 1998.

[55] G. L. Chahine, J. Franc, and A. Karimi, "Laboratory Testing Methods of Cavitation Erosion," in *Advanced Experimental and Numerical Techniques for Cavitation Erosion Prediction*, vol. 106, K.-H. Kim, G. Chahine, J.-P. Franc, and A. Karimi, Eds. Dordrecht: Springer Netherlands, 2014, pp. 21–35.

[56] C. T. Kwok, H. C. Man, and F. T. Cheng, "Cavitation erosion–corrosion behaviour of laser surface alloyed AISI 1050 mild steel using NiCrSiB," *Mater. Sci. Eng. A*, vol. 303, no. 1–2, pp. 250–261, May 2001.

[57] R. J. K. Wood, "Marine wear and tribocorrosion," *Submitt. to Wear Mater.*, 2017.

[58] T. Okada, "Corrosive Liquid Effects on Cavitation Erosion," *J. Ship. Res.*, vol. 25, no. 4, pp. 271–284, 1981.

[59] S. A. Fry and R. J. K. Wood, "The synergistic effect of cavitation erosion and corrosion." Southampton, 1985.

[60] R. Simoneau, J. Fihey, and R. Roberge, "The effect of corrosion in low-intensity cavitation erosion," in *Cavitation Erosion in Fluid Systems*, 1981, pp. 71–81.

[61] Y. Oka and M. Matsumura, "Cavitation erosion-corrosion," in *6th Int. Conference on Erosion by Liquid and Solid Impact*, 1983, p. 11.

[62] Y. Oka, M. Matsumura, and M. Yamawaki, "Slurry erosion-corrosion on commercially pure iron in a vibratory testing facility-mechanism of erosion-corrosion under predominantly erosion conditions," in *7th Int. Coqf on Erosion by Liquid and Solid Impact*, 1987, p. 39.

[63] R. J. K. Wood and S. P. Hutton, "The synergistic effect of erosion and corrosion: published results," *Wear*, vol. 140, pp. 387–394, 1990.